The Astronomical Journal, 162:279 (13pp), 2021 December https://doi.org/10.3847/1538-3881/ac2cc0

What's Behind the Elephant's Trunk? Identifying Young Stellar Objects on the Outskirts of IC 1396*

Steven M. Silverberg[1], Hans Moritz Günther[1], Jinyoung Serena Kim[2], David A. Principe[1], and Scott J. Wolk[3]
[1] MIT Kavli Institute for Astrophysics and Space Research, 77 Massachusetts Avenue, Cambridge, MA 02139, USA; ssilverb@mit.edu
[2] Steward Observatory, Department of Astronomy, University of Arizona, 933 North Cherry Avenue, Tucson, AZ 85721, USA
[3] Smithsonian Astrophysical Observatory, MS 70, 60 Garden Street, Cambridge, MA 02138, USA
Received 2021 June 9; revised 2021 September 10; accepted 2021 September 12; published 2021 December 2

Abstract

Empirically, the estimated lifetime of a typical protoplanetary disk is <5–10 Myr. However, the disk lifetimes required to produce a variety of observed exoplanetary systems may exceed this timescale. Some hypothesize that this inconsistency is due to estimating disk fractions at the cores of clusters, where radiation fields external to a star–disk system can photoevaporate the disk. To test this, we have observed a field on the western outskirts of the IC 1396 star-forming region with XMM-Newton to identify new Class III YSO cluster members. Our X-ray sample is complete for YSOs down to 1.8 $M_{\odot}$. We use a subset of these X-ray sources that have near- and mid-infrared counterparts to determine the disk fraction for this field. We find that the fraction of X-ray-detected cluster members that host disks in the field we observe is 17^{+10}_{-7}% (1σ), comparable with the 29^{+4}_{-3}% found in an adjacent field centered on the cometary globule IC 1396A. We reevaluate YSO identifications in the IC 1396A field using Gaia parallaxes compared to previous color-cut-only identifications, finding that incorporating independent distance measurements provides key additional constraints. Given the existence of at least one massive star producing an external radiation field in the cluster core, the lack of a statistically significant difference in disk fraction in each observed field suggests that disk lifetimes remain consistent as a function of distance from the cluster core.

Unified Astronomy Thesaurus concepts: Protoplanetary disks (1300); Young star clusters (1833); Young stellar objects (1834); X-ray astronomy (1810); X-ray point sources (1270); Star forming regions (1565)

Supporting material: machine-readable table, interactive figure

1. Introduction

Nearby, young stellar clusters are the prime location for studies of the evolution of young stellar objects, specifically the evolution of their circumstellar disks. In the generally accepted model of disk evolution (e.g., Williams & Cieza 2011), pre-main-sequence stars begin their lives surrounded by optically thick protoplanetary disks that accrete material onto their host stars. These objects are categorized as Class I and Class II young stellar objects (YSOs) based on the slopes of their infrared spectral energy distribution (SED; Lada 1987). Over time, these disks evolve and dissipate: photoevaporation, accretion, and the formation of gas giants work in concert to remove much of the gas from the disk, leaving behind a Class III YSO with an optically thin debris disk (e.g., Hughes et al. 2018), or no disk.

Observational studies have shown that the disk fraction in clusters decreases with cluster age (e.g., Haisch et al. 2001; Irwin et al. 2009; Sung et al. 2009) and also correlates with stellar spectral type; later-type stars exhibit a higher frequency of disks than earlier-type stars in the same cluster (e.g., Carpenter et al. 2006). The timescales available for planet formation around young stars are constrained by these timescales for disk dissipation. While previous studies have shown that many primordial disks seemingly dissipate almost too quickly for the epoch of gas-giant formation to occur, on the order of ∼3 Myr (e.g., Irwin et al. 2009; Williams & Cieza 2011), more recent studies have shown that these timescales are closer to 4–5 Myr for late-type stars (e.g., Pecaut & Mamajek 2016), which is slightly more relaxed from what was previously hypothesized. Despite this more relaxed timescale, current empirical disk dissipation timescales still do not entirely align with the prevalence of exoplanets observed in the galaxy (e.g., Fressin et al. 2013; Kunimoto & Matthews 2020).

Pfalzner et al. (2014) hypothesized that the difference in observed disk dissipation timescales and the prevalence of exoplanets is due to observational biases caused by the tendency of disk-frequency studies to focus on the center of clusters, where external radiation fields from massive stars in the cluster core will cause the disks to dissipate more rapidly than if they were in a low-external-radiation environment (e.g., Anderson et al. 2013). Pfalzner et al. (2014) note three biases in particular: (1) because small young clusters will disperse and mix with field stars after a few Myr, studies of clusters at ages 3–10 Myr focus on longer-lived massive clusters, which have a higher fraction of massive stars and thus a lower disk fraction; (2) radiation pressure pushes gas out of the cluster, and a large fraction of members become gravitationally unbound after 1–3 Myr, meaning that most of the remaining members come from the cluster core, where external radiation will dissipate disks more rapidly; and (3) cluster members are more easily identified in the core of a cluster due to the apparent spatial over-density of stars. Additionally, the small field of view of modern telescopes makes obtaining a deep exposure of the full star-forming region infeasible.

* Based on observations obtained with XMM-Newton, an ESA science mission with instruments and contributions directly funded by ESA Member States and NASA.

These factors can combine to produce an underestimate of the true disk fraction in a cluster by focusing on that part of the cluster that intrinsically has a lower disk fraction than the rest of the cluster. To test the hypothesis that the tension in disk dispersal time versus the observed frequency of exoplanets is due to the selection bias of cluster studies, Pfalzner et al. (2014) suggest that adopting a "considerably larger field of view (>20 × 20 pc) in older clusters would in principle reduce this effect." In contrast to this hypothesis, however, Getman et al. (2014) found that the disk fraction decreased as a function of distance from the cluster core in the Orion Nebula Cluster and NGC 2024, which would instead suggest that the outer regions of the cluster are more evolved than the core.

While disk-hosting cluster members are easily identified by their infrared excesses (due to the reprocessing of host starlight by the disk), determining disk fractions requires a robust method of identifying diskless members of young clusters, such as identification by X-ray emission, which is saturated for young stars but decays with age (Preibisch & Feigelson 2005; Booth et al. 2017) such that field stars at the distance of the cluster would no longer be detected. This is commonly used to identify diskless cluster members (e.g., Wolk et al. 2008; Günther et al. 2012).

The H II region IC 1396 is located at the edge of the Cepheus OB2 association, at a distance of 850 pc—1 kpc (Contreras et al. 2002; Sicilia-Aguilar et al. 2019). The central O star binary, HD 206267, ionizes the H II region, driving a shock front into the surrounding molecular cloud. HD 206267 is also the center of the 3.7 Myr open cluster Tr 37 (Kun et al. 2008 and references therein), which is devoid of gas. HD 206267 has been the subject of several X-ray observations, which have been used to identify cluster members (Mercer et al. 2009; Getman et al. 2012). Three individual small globules in the region have also been observed (Getman et al. 2007, 2012), finding evidence of triggered star formation in the globules separate from the population of young stars associated with the open cluster Tr 37—for instance, the stellar population associated with the cometary globule IC 1396A is thought to be ∼1 Myr old (Getman et al. 2012) More than 800 members of the Tr 37/IC 1396 cluster have been identified through the use of X-ray observations (Mercer et al. 2009; Getman et al. 2012), spectroscopic surveys (Contreras et al. 2002; Sicilia-Aguilar et al. 2006a, 2013), infrared disk searches (Reach et al. 2004; Sicilia-Aguilar et al. 2006b; Morales-Calderón et al. 2009), and Hα photometry (Barentsen et al. 2011).

In this paper, we present X-ray detections from an 87.3 ks exposure of the outer part of IC 1396, west of the core of the Trumpler 37 cluster and near the "base" of the Elephant's Trunk Nebula, with XMM-Newton. For convenience, we refer to this field as IC 1396-West (or IC 1396W) for the rest of the paper. We show the location of these observations relative to other X-ray observations of the region and the underlying nebular dust background in Figure 1. We use these data, in conjunction with archival optical, near-infrared, and astrometric data to identify likely members of the cluster. We identify striking patterns in the locations of young stars along the apparent edges of the dust clouds (as shown in WISE mid-infrared data). We also use this archival data in conjunction with previous observations of an adjacent region observed with Chandra/ACIS-I centered on the cometary globule IC 1396A to compare our methods for disk identification to those of Getman et al. (2012).

2. Observations and Data Reduction

2.1. XMM-Newton

We obtained an 87.3 ks observation of the western outskirts of IC 1396 beginning on UT 2015 December 1 (XMM-Newton observation 0762360101). This observation was designed to observe the outer part of the cluster behind the "base" of the Elephant's Trunk (the region highlighted in blue in Figure 1), specifically for purposes of identifying Class III sources. The observations used the medium-thickness optical blocking filter. We used the pipeline reduction of these data produced as part of the full reprocessing of the XMM-Newton archive for the 4XMM catalog in 2019.[4] Because there were no particularly bright targets in the center of the field of view, we do not incorporate data from either RGS camera. The reduction detects 152 X-ray sources.

2.2. Near-infrared Imaging from UKIRT

A square degree of IC 1396 was monitored with the Wide-Field Camera (WFCAM) on the United Kingdom Infrared Telescope (Casali et al. 2007) over 21 epochs from 2014 July 18 to 2016 July 12, first presented in Meng et al. (2019). While that work looked at variability between epochs, we use here the combined photometry across all 21 epochs, which allows us to obtain deeper photometry than that provided by the Two Micron All-Sky Survey (2MASS; Skrutskie et al. 2006). Seeing ranged from 0.″6 to 1.″4, with average seeing of 0.″79. We refer the reader to Meng et al. (2019) for details on the observations and reduction of this data. The pipeline-reduced data, which we use here, are available in the database WSERV9v20170222, at the WFCAM Science Archive[5] (Hambly et al. 2008).

We noticed in our comparison of data that the use of the star/galaxy probabilities provided by the WFCAM pipeline to eliminate sources without high probabilities of being stars (as was done in Meng et al. 2019) produced an underdensity of sources identified as stars along the path of the dust bands observed in the WISE data, without a corresponding drop in the number of sources overall along the dust band but with a drop in a number of total sources behind the cometary globule at the center of IC 1396A. This most clearly appears when comparing the ratio of objects that are classified as stars in each spatial bin to the total number of objects in each bin, shown in Figure 2. This suggests that the automated classification of star versus galaxy was affected by the dust (either due to foreground dust reddening the stars into colors more typically found in galaxies, or background dust producing a less defined point source). We therefore make no cuts based on the automated classification of each object in the UKIRT/WFCAM pipeline. We note the duplication of some sources in the overlap between regions observed at different times due to imperfect source matching; these observations typically had consistent (within uncertainties) photometry with each other at very low separations and came from different frame sets, suggesting that the sources were multiple detections of the same source. To eliminate these, we matched the UKIRT data set to itself with a search radius of 0.″5, below the typical spatial resolution of the observations, and for each set of duplicated sources selected one source identifier as the "true" source.

[4] A custom configuration based on SAS version 18.0.0.
[5] http://wsa.roe.ac.uk/

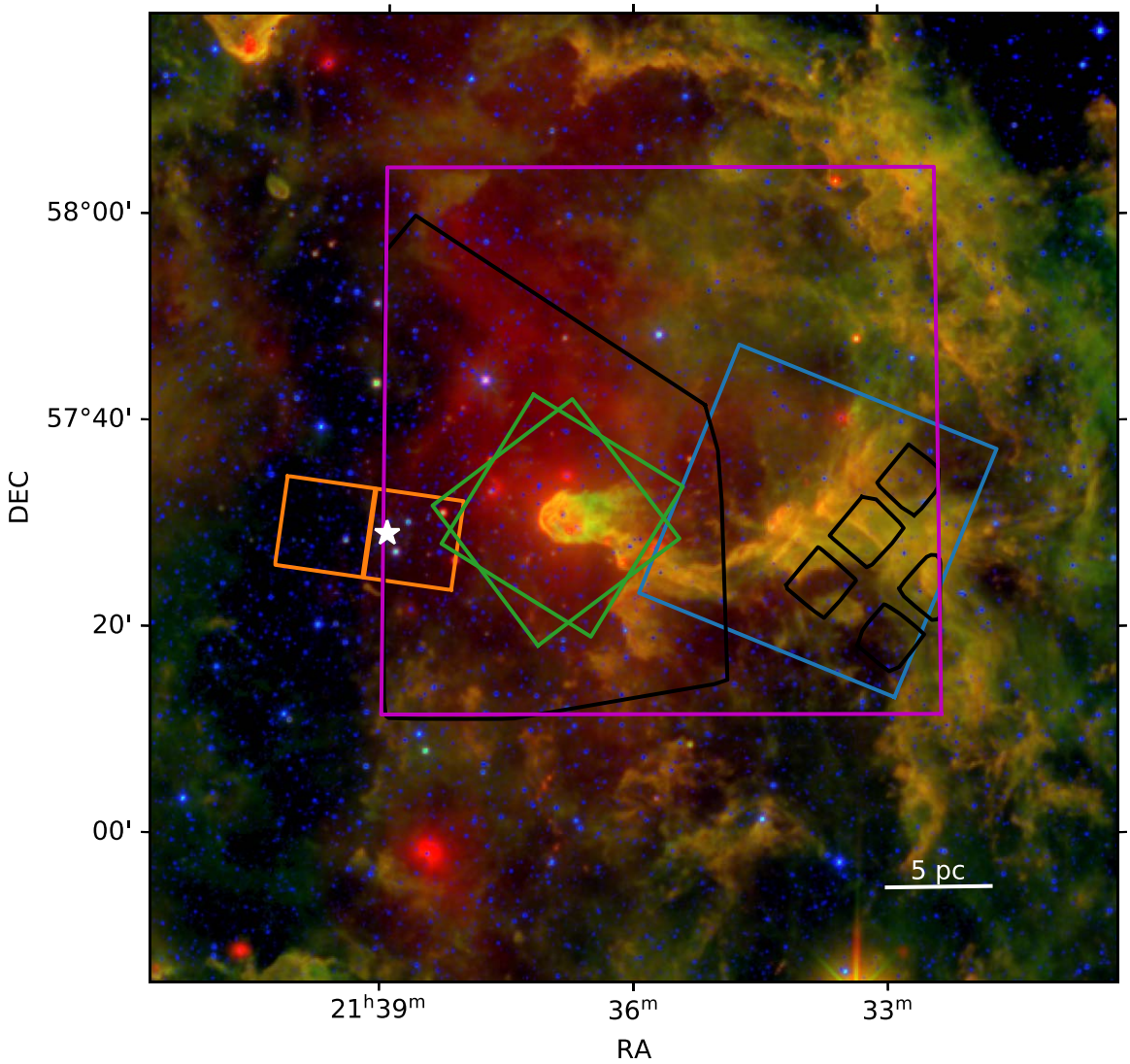

Figure 1. Selected X-ray and mid-IR pointings toward IC 1396, the Elephant Trunk nebula. The background is a false-color combination of the W1 (blue), W3 (green), and W4 (red) channels from the Wide-field Infrared Survey Explorer (WISE). Chandra/ACIS-I pointings toward the globule at the "tip" of the trunk (Getman et al. 2012) are outlined in green. The orange outline shows the alignment of the inner two Chandra/ACIS-S chips, analyzed in Mercer et al. (2009). The blue outline shows the alignment of the XMM-Newton PN camera during the new observations presented here. The MOS detectors cover a similar field of view. The blue points are point sources that are resolved in W1. The area covered by the UKIRT/WFCAM observations is outlined in magenta. Black outlines indicate the areas within the UKIRT/WFCAM field that are covered by at least one Spitzer/IRAC band. The white star indicates the position of HD 206267, the spectroscopic O-star binary at the heart of this region.

2.3. Archival Data

We retrieved photometry of the region observed in the UKIRT data from the early third data release from ESA's Gaia mission (Gaia EDR3; Gaia Collaboration et al. 2016, 2021), the AllWISE catalog of data from the Wide-field Infrared Survey Explorer (WISE; Cutri et al. 2021), and various pointed observations with the Spitzer Space Telescope (Werner et al. 2004), obtained via the Spitzer Heritage Archive.

We use the UKIRT/WFCAM and 2MASS data as the backbone of our target matching. We searched the Spitzer Catalog for point sources matching the coordinates of our near-IR sources with a search radius of 1″, chosen based on the typical 0.″8 seeing of the UKIRT data and the Spitzer point-spread function, yielding 19,744 sources. We then crossmatched the near-IR data set with Gaia EDR3 and AllWISE using the CDS xMatch functionality as implemented in `astroquery` (Ginsburg et al. 2019), again using a search radius of 1″ for consistency with the Spitzer crossmatch.

Finally, we used the CDS xMatch service to match the XMM and UKIRT/2MASS objects, with a match radius of 2″ because the point-spread function (PSF) of XMM-Newton is considerably wider than the UKIRT and 2MASS PSFs. We examined by hand each of the matches between the XMM-Newton and UKIRT sources to determine its relevance to our work (e.g., identifying the UKIRT source most likely to correspond to the X-ray data in cases where there were two or more UKIRT sources matched to the same X-ray source). The XMM field is aligned such that some of the field falls outside the region for which we have WFCAM data; we thus do not consider the six X-ray sources that fall outside of this range.

There are 47 X-ray sources in the XMM-Newton observation without UKIRT/WFCAM counterparts. While most of these are likely extragalactic in origin, several are among the

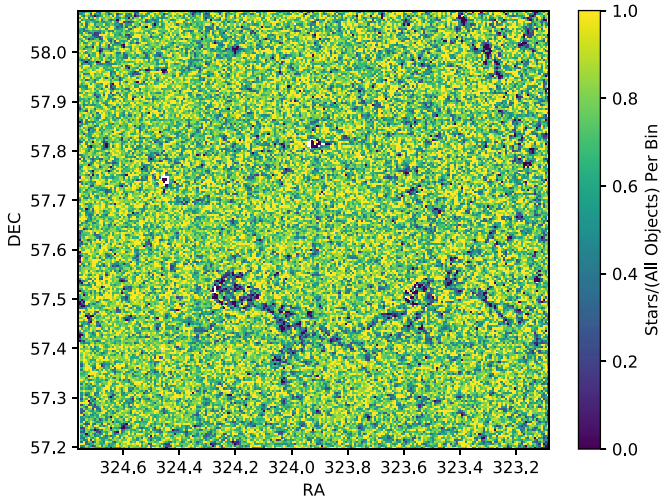

Figure 2. The ratio of objects classified as stars by the WFCAM pipeline to all objects shows that the fraction of objects labeled stars is generally constant with the exception of the Elephant Trunk nebula. This suggests that the difference is that the pipeline classifies objects differently in the region of the nebula. The faint grid pattern is due to source duplication from imperfect matching between observation sets.

brightest X-ray sources, suggesting that they are Galactic in origin. To check if these X-ray sources had near-IR counterparts too bright for UKIRT/WFCAM, we also crossmatched the XMM-Newton data to 2MASS. However, we found that all XMM/2MASS matches in the UKIRT field also had UKIRT matches, suggesting that UKIRT saturation was not the cause of the lack of a near-IR counterpart.

To compare our sample to other studies of this region, we also crossmatched X-ray sources from Chandra/ACIS-I images of the cometary globule IC 1396A at the tip of the elephant's trunk (Getman et al. 2012) to the UKIRT data, again using the CDS/Xmatch functionality. For convenience, we refer to this field as IC 1396A for the remainder of the paper. While this field does not cover the core of the Tr 37 cluster (which presumably formed out of the IC 1396 molecular cloud), it is more interior to the cluster than the IC 1396-West field. We do not examine X-ray data from the cluster core (Mercer et al. 2009) because these Chandra data have diminished sensitivity due to the presence of the Chandra High-Energy Transmission Grating Spectrometer (HETG-S) and because the UKIRT field does not fully overlap with the cluster core. Considering just the IC 1396A field and the IC 1396-West fields provides near-complete coverage of the Elephant's Trunk from tip to where it meets the larger cloud, as depicted in Figure 1. We used the crossmatches to 2MASS identified by Getman et al. (2012) for those X-ray sources that did not have a UKIRT counterpart.

2.4. Estimating the Cluster Distance with Gaia EDR3

We estimated the distance to the cluster using Gaia EDR3 parallaxes to cluster members that have previously been identified via a variety of methods (Contreras et al. 2002; Sicilia-Aguilar et al. 2005b, 2006a, 2013; Reach et al. 2004; Morales-Calderón et al. 2009; Barentsen et al. 2011; Sicilia-Aguilar et al. 2006b; Mercer et al. 2009; Getman et al. 2012), following the methodology of Sicilia-Aguilar et al. (2019). As with Sicilia-Aguilar et al. (2019), we selected only those sources that had matching radii $<0\farcs5$, relative parallax uncertainties with a ratio of parallax uncertainty to parallax $\sigma_\omega/\omega < 0.1$, and proper-motion uncertainties below 2 mas yr^{-1}, to ensure that the Gaia source was the same as the source in the existing catalog. We also required that for those objects that had both Gaia DR2 and EDR3 parallax measurements, the estimated distance from EDR3 is consistent with its estimated distance from Gaia DR2; this ensures that any differences in our estimate relative to Sicilia-Aguilar et al. (2019) are due to incorporating sources with new or improved-quality parallax measurements, rather than potential mismatches with Gaia EDR3. We estimated distances following the prescription of Bailer-Jones (2015), using a characteristic length scale of $l = 1.35$ kpc in the prior based on the direction of observation (Bailer-Jones et al. 2018).

We found an average distance to the cluster of 931^{+159}_{-116} pc, where the uncertainties indicate the 5th and 95th percentiles. This measurement is consistent with both the Sicilia-Aguilar et al. (2019) estimate of 945^{+90}_{-73} pc[6] and the previous value of 870 pc from Contreras et al. (2002). We note that our work here specifically does not incorporate additional information beyond a literature identification of cluster membership and a parallax measurement; future work that incorporates more information from Gaia (e.g., proper-motion measurements) will likely produce a more precise result. However, this distance estimate will be sufficient for our purposes: excluding objects with distances that are inconsistent with cluster membership from our sample.

3. Classifying YSOs

Disks and circumstellar material are apparent as IR excess because the circumstellar material absorbs and reradiates the stellar emission. The disk temperature decreases with distance from the star; thus, the SED typically peaks at a few microns for disk sources, and at longer wavelengths for Class I sources, which are still embedded deep in their envelope. To assess the presence of a disk for each near-IR source with Spitzer or AllWISE data, we determine the exponent α in a power-law fit to each object's spectral energy distribution (SED; e.g., Figure 3), starting with the near-IR H band from UKIRT/WFCAM, using maximum-likelihood estimation. We computed separate estimates for α based on Spitzer/IRAC data and AllWISE data, trading AllWISE's spatial coverage for the improved sensitivity of IRAC. Based on the full-frame images in AllWISE, we found that the 12 and 22 μm AllWISE data primarily detect the background emission from the nebula; we thus only used data from wavelengths shorter than 10 μm. We separate sources into YSO classes based on the boundaries on power-law fitting classifications outlined by Williams & Cieza (2011): Class I objects have power laws with exponents $\alpha > 0.3$; Class FS (flat-spectrum) objects have $0.3 > \alpha > -0.3$; Class II objects have $-0.3 > \alpha > -1.6$, and Class III objects have $\alpha < -1.6$. While there are some degeneracies between classes (e.g., a Class II YSO viewed from high inclination can have a similar SED to a typical Class I YSO; Robitaille et al. 2006), this method provides a simple categorical assessment of the presence of circumstellar material without potentially overfitting the data, as might happen with a more elaborate disk model. Example SEDs of each class are

[6] We note that the value quoted here incorporates an additional prior to identify the highest-likelihood members to enable a proper-motion study in Sicilia-Aguilar et al. (2019). Removing this prior yields a distance 949^{+161}_{-101} pc (A. Sicilia-Aguilar 2021, private communication), with uncertainties in line with those presented above.

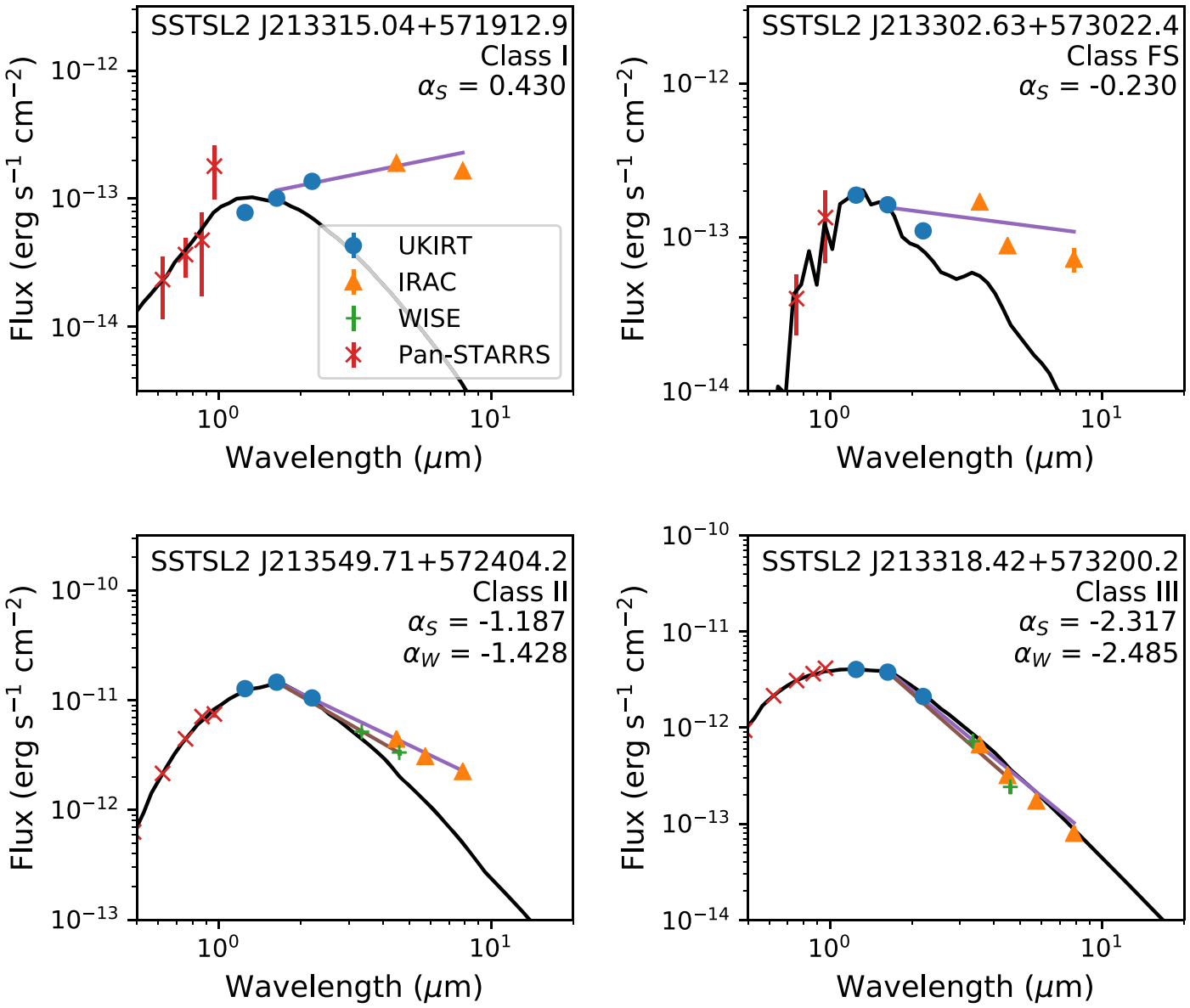

Figure 3. Example SEDs of each class of YSO. A photosphere-only model from Robitaille (2017) is plotted in black for comparison. The best-fit power law to the Spitzer data is shown in purple, while the best-fit power law to the AllWISE data (where available) is in brown. Error bars represent 3σ uncertainties; these are typically too small to be seen in the UKIRT and Spitzer data.

shown in Figure 3. In cases where an object had both Spitzer and WISE data, we use the Spitzer-derived value for α, as WISE data are more likely to suffer from blends with nearby sources and extended cloud emission due to its larger PSF (e.g., Kennedy & Wyatt 2012; Kuchner et al. 2016; Silverberg et al. 2018). We summarize our filtering procedure in Table 1.

Class III objects were initially identified as sources with SEDs that correspond to a stellar photosphere ($\alpha < -1.6$) that also emit X-rays (indicative of youth) and had a parallax per Gaia EDR3 that placed them at the correct distance. Only 13 Class III sources at the correct distance per Gaia EDR3 were detected in the XMM data. Removing the Gaia requirement while keeping the requirements on α and the presence of X-rays added an additional two sources.

In addition to assessing the slope of the objects' SEDs, we made additional cuts based on data from Gaia EDR3, using the cluster distance estimate we derived in Section 2.4. We initially selected only those objects with Gaia-measured parallaxes with distances whose 90% confidence intervals (following Bailer-Jones 2015; Sicilia-Aguilar et al. 2019) overlap with the 90% bounds identified in Section 2.4 for the cluster to provide an independent constraint on what objects are or are not likely cluster members. We found that several sources along the boundary of the nebula do not have Gaia parallaxes, which we expect is due to the combined effects of potential binarity, additional fuzziness of the images due to the background nebula, and incompleteness of Gaia at these distances. We expect that many of these sources for which there is not a published parallax measurement from Gaia will be included in future Gaia releases. In the meantime, we assume that those objects that do not have Gaia-parallax measurements but do have SED slopes indicative of a disk are associated with the nebula and the cluster, and thus include them in our measurements.

We map the locations of the YSOs identified in this sample in Figure 4. We find that 5707 UKIRT sources with matched

Spitzer or WISE photometry in the IC 1396-West field have distances based on Gaia EDR3 parallaxes that are outside the cluster bounds derived in Section 2.4, leaving 1356 UKIRT sources with WISE or Spitzer photometry to consider as potential cluster members. We will consider the sources with Spitzer and WISE data separately in each of the following sections.

3.1. Results with Spitzer

A total of 213 sources with Spitzer photometry have $\alpha_S > -1.6$ from Spitzer. Of these, 174 have α_S values that correspond to Class II YSOs, while 25 have slopes corresponding to Class FS and 14 have slopes corresponding to Class I. We list these in Table 2. One of these sources is also detected with XMM-Newton.

Three hundred forty-five sources with mid-IR data from Spitzer or WISE have SED slopes corresponding to a bare photosphere ($\alpha \leq -1.6$) and Gaia-parallax-based distances that place them at the correct distance for cluster membership, while an additional 491 have SED slopes corresponding to a bare photosphere and no parallax measurement. Of these, 15 also have X-ray detections with XMM-Newton, making them Class III YSO candidates. We list these in Table 2. The others require additional observational data, such as deeper X-ray observations or the detection of lithium in their spectra, to determine their youth.

3.2. Assessing Confusion and Contamination with AllWISE

A total of 288 sources have $\alpha > -1.6$ from AllWISE. We checked each of these sources that did not also have Spitzer data to determine whether the source was likely to be blended, contaminated, or confused, based on whether it was matched to multiple UKIRT sources using the 1″ search radius. We excluded any UKIRT sources for which the same AllWISE source was matched to multiple UKIRT sources. This leaves 153 sources with $\alpha_W > -1.6$ that we believe to be uncontaminated. Of these, 72 have SED slopes corresponding to Class I; 26 have SED slopes corresponding to Class FS; and 55 have SED slopes corresponding to Class II. Two of these sources (one Class FS YSO, and one Class II YSO) are also detected with XMM-Newton. These are listed in Table 2.

We expect that there will be some differences between detections with WISE and Spitzer, due to differences in the WISE and Spitzer PSFs, observation strategies (Spitzer provides deeper observations at the expense of spatial coverage), and data reduction (e.g., background subtraction).

To check whether we could reasonably combine estimates of α from Spitzer and AllWISE, we considered the 105 sources in IC 1396-West that are detected with both telescopes. Of these, 99 have α in each telescope that corresponds to the same YSO class. Two Class II sources in Spitzer have Class III slopes in WISE, and one system has a Class II slope in Spitzer but a Class FS slope in AllWISE. Most notably, three sources with α_S corresponding to Class III have α_W corresponding to disk-hosting classes—i.e., three Class III sources are misclassified as disk hosts using WISE data. If we assume similar statistics hold for the rest of the field, $95.2^{+1.7}_{-2.5}$% of YSO classifications in the AllWISE-only sample would be classified the same way by Spitzer, indicating that we can reliably compare results from each telescope despite their differences.

Table 1.
Filtering Procedure for Identifying YSOs

Categorization	Number of Sources
UKIRT Sources with Spitzer or WISE Crossmatches	6537
Sources outside the Cluster Distance per Gaia	(5181)
Remaining Sources	**1356**
Spitzer Sources	780
UKIRT Sources Matched to Identical Spitzer Sources[a]	(18)
Remaining Spitzer Sources	**762**
Spitzer Sources with $\alpha_S \geqslant -1.6$	213
Class I	14
Class FS	25
Class II	174
Spitzer Sources with $\alpha_S < -1.6$	549
AllWISE-only Sources	576
UKIRT Sources Matched to Identical AllWISE Source[a]	(136)
Remaining AllWISE Sources	**440**
AllWISE-only Sources with $\alpha_W \geqslant -1.6$	153
Class I	72
Class FS	26
Class II	55
AllWISE Sources with $\alpha_W < -1.6$	287
Sources with $\alpha_{S,W} < -1.6$	836
Sources with $\alpha_{S,W} < -1.6$ at Cluster Distance	345
Sources with $\alpha_{S,W} < -1.6$ Without Parallax Measurement	491
Remaining Sources with XMM-Newton Detections	18
Disk Hosts Detected with XMM-Newton	3
Spitzer-detected Disk Hosts with XMM-Newton Detections	1
AllWISE-detected Disk Hosts with XMM-Newton Detections	2
Class III Candidates Detected with XMM-Newton	15
Class III Candidates at Cluster Distance with XMM-Newton Detections	13
Class III Candidates without Parallax Measurements with XMM-Newton Detections	2
UKIRT Sources Without Spitzer or WISE Crossmatches Detected in X-rays[b]	40

Notes.
[a] This refers to the case where more than one UKIRT source is matched to a given Spitzer or AllWISE source. In these cases, because we typically cannot determine whether one source is the "correct" match or if the mid-IR data is a blend of the two near-IR sources, we remove the UKIRT source from consideration.
[b] This notes UKIRT sources without Spitzer or WISE crossmatches that were detected with XMM-Newton and either Gaia parallaxes that put them at the cluster distance, or no Gaia-parallax measurement.

3.3. X-Ray-detected Cluster Members with Mid-IR Data

Fifteen UKIRT/WFCAM sources with mid-IR matches and $\alpha < -1.6$ are detected with XMM-Newton, as are three UKIRT/WFCAM sources with mid-IR matches and $\alpha > -1.6$. These are listed in Table 2. This yields a disk fraction for X-ray-detected cluster members of 17^{+10}_{-7}%, comparable within uncertainties to both the 29^{+4}_{-3}% claimed by Getman et al. (2012) for the IC 1396A field between IC 1396-West and the core, and to the 20^{+10}_{-7}% disk fraction for X-ray-detected cluster members in the core of the Tr 37 cluster by

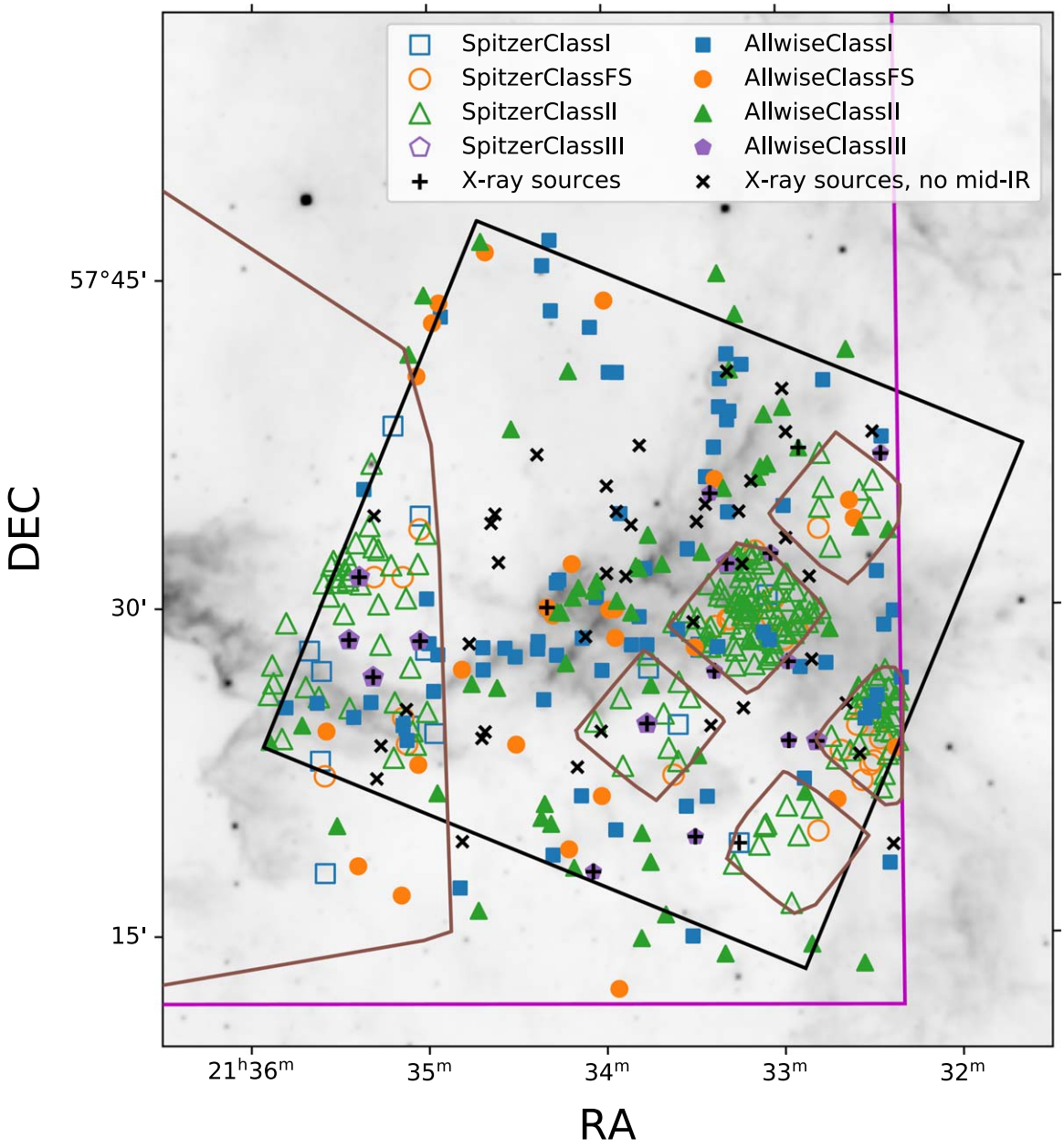

Figure 4. YSOs identified in the field of view of XMM-Newton observations of the outskirts of IC 1396. The background is the 12 μm image of the region from WISE. The field of the XMM-Newton PN camera is outlined in black, while the UKIRT field is outlined in magenta. While more sensitive, Spitzer observations are confined to specific pointings. Individual Spitzer/IRAC pointings are indicated in brown. A subset of AllWISE-identified YSOs clearly fall along the nebula-wise dust lane concentrated in the center of the XMM-Newton field. Class II is by far the most common classification. Interactive figure available; source classes can be interactively selected and deselected to improve visibility in dense regions, and sources are tagged individually with the source ID, coordinates, α, and X-ray flux.

Mercer et al. (2009). The uncertainties on these disk fractions were determined using the Wilson score interval for uncertainty in binomial proportions (Wilson 1927) with $z = 1$. In summary, between disk-hosting sources that we detect in the archival data and the Class III sources detected with XMM-Newton, we identify 381 new YSOs in IC 1396 with mid-IR data.

4. Discussion

4.1. Completeness of Our Sample

Many factors limit our ability to effectively identify all cluster members in the region where IC 1396-West overlaps with the UKIRT/WFCAM data. Higher-mass stars are intrinsically brighter than their lower-mass counterparts, making them more detectable in X-rays. This is compounded by the suppression of X-ray emission due to accretion in disk hosts, as higher-mass stars dissipate their disks more quickly than their lower-mass counterparts (e.g., Carpenter et al. 2006). An X-ray-selected sample is thus biased toward higher-mass stars, which are more likely to be diskless, resulting in a disk fraction lower than the true disk fraction for the region.

Simply identifying additional disk hosts provides another observational bias. The SED of a disk host is fairly conspicuous even in faint mid-IR data, such that we can detect a disk around a low-mass star just as readily as around a high-mass star. Similarly, a disk indicates youth just as readily as X-ray emission, so we can readily identify disk-hosting low-mass

Table 2.
YSOs in the XMM-Newton Field of View

Num	Label	Description	Units
1	catUKIRT	UKIRT Source ID. Should be preceded by "44994077."	⋯
2	catSpitzer	Spitzer source ID	⋯
3	catWISE	WISE source ID	⋯
4	R.A.	R.A. (J2000) of UKIRT source	degrees
5	decl.	decl. (J2000) of UKIRT source	degrees
6	plx	Gaia EDR3 parallax	mas
7	plxerr	Uncertainty on Gaia EDR3 parallax	mas
8	Jmag	UKIRT/WFCAM *J* magnitude	mag
9	Jmagerr	Uncertainty of UKIRT/WFCAM *J* magnitude	mag
10	Hmag	UKIRT/WFCAM *H* magnitude	mag
11	Hmagerr	Uncertainty of UKIRT/WFCAM *H* magnitude	mag
12	Kmag	UKIRT/WFCAM *K* magnitude	mag
13	Kmagerr	Uncertainty of UKIRT/WFCAM *K* magnitude	mag
14	I1flux	Spitzer/IRAC *I1* flux	μJy
15	I1fluxerr	Uncertainty of Spitzer/IRAC *I1* flux	μJy
16	I2flux	Spitzer/IRAC *I2* flux	μJy
17	I2fluxerr	Uncertainty of Spitzer/IRAC *I2* flux	μJy
18	I3flux	Spitzer/IRAC *I3* flux	μJy
19	I3fluxerr	Uncertainty of Spitzer/IRAC *I3* flux	μJy
20	I4flux	Spitzer/IRAC *I4* flux	μJy
21	I4fluxerr	Uncertainty of Spitzer/IRAC *I4* flux	μJy
22	W1mag	WISE W1 magnitude	mag
23	W1magerr	Uncertainty of WISE W1 magnitude	mag
24	W2mag	WISE W2 magnitude	mag
25	W2magerr	Uncertainty of WISE W2 magnitude	mag
26	alphaS	Spitzer-derived SED slope α_S	⋯
27	alphaW	WISE-derived SED slope α_W	⋯
28	class	Adopted YSO class	⋯
29	xrayflux	Combined (EPIC) X-ray flux (0.2–12 keV)	erg s^{-1} cm^{-2}
30	xrayfluxerr	Uncertainty on combined X-ray flux	erg s^{-1} cm^{-2}
31	HR	Hardness ratio	⋯
32	HRerr	Uncertainty on hardness ratio	⋯
33	PrevId	Previous references to this source	1, 2, 3[a]

Note. Machine-readable versions of the full table are available. Here, we list the columns and descriptions of the data in that table.
[a] References: (1) Getman et al. (2012); (2) Barentsen et al. (2011); (3) Sicilia-Aguilar et al. (2005a)

(This table is available in its entirety in machine-readable form.)

Table 3.
Predicted Characteristics of a 1.0$M_\odot$ YSO at Various Extinction Levels

A_V	N_H (10^{21}cm^{-2})	Count Rate (cts s^{-1})	Magnitudes			
			V	*K*	*I2*	*W2*
0	0	3.0×10^{-2}	15.7	12.8	12.77	12.76
1.56	3.5	1.1×10^{-2}	17.3	13.0	12.85	12.84
5	11.1	3.8×10^{-3}	20.7	13.4	13.03	13.01
10	22.1	1.4×10^{-3}	25.7	14.0	13.30	13.27
20	44.2	5.2×10^{-4}	35.7	15.2	13.82	13.78

stars without X-ray emission. However, only including sources with either an X-ray detection or a disk biases our search heavily in favor of finding a disk fraction larger than the true disk fraction, as this would include the low-mass disk hosts while excluding the low-mass non-disk hosts.

Additionally, the effects of the surrounding nebula could lead to misidentification of an embedded cluster member as a background extragalactic source. We can illustrate this by considering the case of a hypothetical single 1.0 $M_\odot$ YSO at 1000 pc (within the expected range for cluster distance, but further toward the back of the cluster), at varying levels of extinction (and thus varying degrees of interstellar absorption). We use the colors of a 1.0 $M_\odot$ pre-main-sequence star from Pecaut & Mamajek (2013) and assume an unabsorbed flux for a 1.0 $M_\odot$ weak-lined T Tauri star from the $L_X - M$ relationship of Telleschi et al. (2007), following an APEC model with $\log(T) = 7.05$. We assume for illustrative purposes the relationship between column density N_H and A_V from Güver & Özel (2009): $N_H = (2.21(\pm 0.09) \times 10^{21})A_V$. In Table 3, we present five cases for this source: no foreground material, the typical cluster extinction per Sicilia-Aguilar et al. (2005b), and $A_V = 5$, 10, and 20, corresponding to varying levels to which the source is still embedded in its natal envelope. As these demonstrate, a YSO could be faint enough to go undetected in *V*-band observations, and on the borderline of detection in the UKIRT/WFCAM *K* band, while still producing detectable X-rays. This could account for some portion of detected X-ray sources without a near-IR counterpart.

More subtly, relying on Spitzer data leaves us only with data in the specific pointings available. While it has more spatial coverage, AllWISE is also magnitude limited. Heavily extincted sources may thus go undetected in IR, while their X-rays are detected as hard sources without an IR counterpart and interpreted as a background AGN. The wide PSF of AllWISE ($\sim 6''$ at W2; Wright et al. 2010) also means that inevitably several potential good disk candidates are removed from consideration due to confusion and contamination (see Section 3.2).

Astrometry, independent of X-ray and IR emission, could potentially be used to identify cluster members—ideally, we would be able to map the bulk motion of known cluster members and then algorithmically find objects with similar motions. However, Gaia EDR3 is only complete to a magnitude limit $G = 17$ (Gaia Collaboration et al. 2021), with a poorly defined faint limit beyond that; if we conservatively assume incompleteness below $G = 17$, an extinction $A_G \simeq 2$, and a distance to the cluster of 931 pc, Gaia data will be incomplete for cluster members with $M_G \gtrsim 5.2$. This would bias the sample both toward targets at the front of the cluster (i.e., at distances < 931 pc) due to their higher apparent brightness and minimized extinction from the nebula, and toward intrinsically brighter (i.e., high-mass) sources.

While the issues all combine to provide an incomplete picture of the cluster in this region, it is worth noting that past surveys should suffer from similar issues for similar reasons. We thus conclude that our search with X-rays is broadly comparable to past X-ray-based searches for cluster members in IC 1396. For the purposes of estimating the disk fraction of cluster members, we focus on the X-ray-detected cluster members, as this is the surest way to ensure that we are comparing similar subpopulations of the cluster. We acknowledge that this disk fraction estimate is at best a lower limit on the true disk fraction of the cluster, given the number of low-mass stars we do not consider here; however, it is the best

estimate available with the data we have in hand. While we do not incorporate the disk-hosting YSOs we identify that are not detected in X-rays into our disk fraction estimate, we present their identification here so that a more accurate disk fraction can be computed as more complete data sets become available.

4.2. Remaining X-Ray Sources

Only 18 of the 152 X-ray sources in IC 1396-West are identified clearly as disk-hosting or non-disk-hosting cluster members. While 6 of the remaining 134 are not included because they do not overlap with the UKIRT/WFCAM observations, it behooves us to consider the remaining 128 sources.

Forty-seven XMM sources in the UKIRT field have neither a UKIRT nor 2MASS counterpart within 2″. We expect that these are likely either extragalactic sources, or cluster sources embedded deep enough within the nebula that they are undetected in UKIRT due to extinction. For the full XMM-Newton/EPIC field of view, we would expect ∼78 extragalactic background sources with fluxes $>2.5\times10^{-14}$ erg s^{-1} cm^{-2} (Moretti et al. 2003); our number of 47 unmatched sources in the UKIRT/XMM overlap region (more than half of the full field of view) is consistent with that number. We do not detect as many sources that can be interpreted as extragalactic background sources as were found in the IC 1396A field (Getman et al. 2012); we expect that this is due to the apparent higher column density of the nebula in IC 1396-West compared to the IC 1396A field (Figure 1), the higher background level for XMM-Newton compared to Chandra, the larger PSF for XMM-Newton resulting in faint background sources going unresolved, and the lower sensitivity threshold we find for the XMM-Newton observations compared to the Chandra observations (Section 4.4).

Fifty-five XMM sources have UKIRT counterparts that either do not have matches to Spitzer or AllWISE sources or do not have a valid slope solution. Of these, 16 have Gaia-parallax measurements that put them outside the cluster, while 2 have parallaxes that put them within the cluster and 38 have no measured parallaxes. These 40 sources (two with in-cluster parallaxes, 38 without measured parallaxes) are likely cluster members, bringing the total number of YSOs we identify to 421, but we lack sufficient data to determine if they host disks or not.

Twenty-three XMM sources have UKIRT counterparts and matches to Spitzer or AllWISE, but have Gaia parallaxes that put them outside the cluster. These are a mix of 12 foreground sources, 2 background sources, and 9 sources where the range between the 5th and 95th percentile values of the distance distribution exceeds 1000 pc. The nine sources with highly uncertain distance estimates are almost certainly background sources; however, in some cases, their highly uncertain distance estimates overlap with the distance estimate for the cluster, so they are treated separately.

This leaves 20 sources with UKIRT matches, Spitzer or AllWISE data matched to the UKIRT source, and a parallax that does not exclude them from the cluster. In two of these cases, the AllWISE match is matched to more than one UKIRT source, and these are thus excluded (as in Section 3.2), to produce our final sample of 18.

It is worth noting that the distributions of the near-IR (*K*-band) brightness of the X-ray-detected cluster members with and without mid-IR data are distinct. The sources with

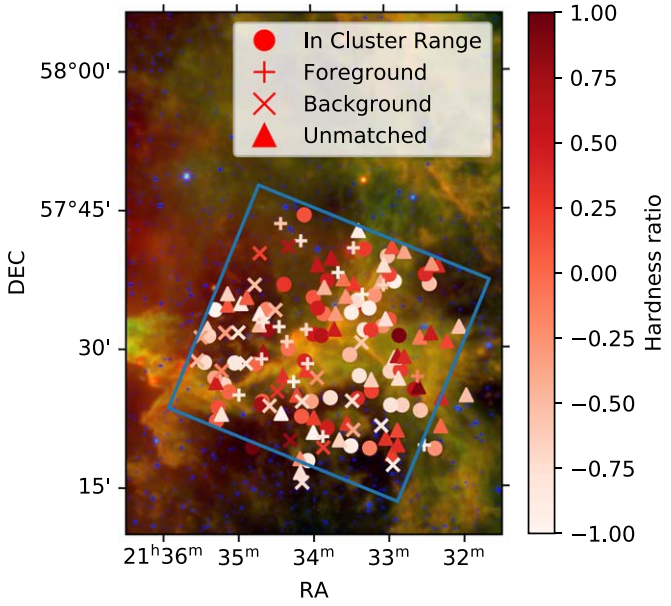

Figure 5. Hardness ratios as measured by XMM-Newton. The color gradient indicates the hardness ratio from white (soft) to red (hard). Different markers indicate objects in different categories based on distance derived from Gaia EDR3: in range for cluster membership, foreground, background, and sources for which Gaia does not provide useful information (sources that are undetected, do not have a measured parallax, or which have a distance with uncertainty greater than 1000 pc.

mid-IR data are in general much brighter—the median UKIRT/WFCAM *K* magnitude of the sources with mid-IR data is 12.539, while the median *K* magnitude for the sources without mid-IR data is 18.304. This is not overly surprising, as one would expect brighter sources to be those detected with WISE in the regions where Spitzer data is unavailable. It does, however, indicate that the sources without mid-IR data are likely of lower mass than the sources with disks, likely are at the far side of the cluster rather than the near side, and thus likely are more embedded in the nebula as well.

To evaluate these X-ray sources independently of their match to UKIRT, we computed hardness ratios for each source, using the broad bands defined in the XMM-Newton pipeline (band 6 = 0.2–2 keV; band 7 = 2–12 keV):

$$HR = \frac{B_H - B_S}{B_H + B_S}, \tag{1}$$

where $B_{H,S}$ are the count rates in the hard and soft bands, respectively. These are shown in comparison to the WISE image in Figure 5.

As expected, foreground sources are the softest sources. The background sources are not exclusively hard, though this varies positionally, with softer background sources appearing at areas of minimal dust emission, as expected for Galactic background sources. The cluster members show a wide variety of hardnesses; some are among the hardest sources in the field. These appear to be spatially coincident with the star-forming nebular cloud; harder cluster members typically fall along the dust band, indicating a higher degree of embeddedness. The unmatched sources vary in hardness as well, with some soft sources appearing in regions of low nebular emission, as well as the harder emission expected of extragalactic sources. The appearance of a set of soft unmatched sources along the nebula as it branches to the northwest (starting at approximately R.A.

$21_h33_m42_s$ and decl. 57°32′06″) suggests a potential additional population of cluster members that are not detected in the infrared data, either due to extinction from the nebula or intrinsic faintness.

4.3. Distribution of Cluster Members through the Nebula

We find that only 17^{+10}_{-7}% of likely cluster members in the IC 1396-West field with X-ray detections and available mid-IR data have disks. While this is not statistically different from the 29^{+4}_{-3}% found by Getman et al. (2012) or the 20^{+10}_{-7}% found by Mercer et al. (2009), it qualitatively suggests that the disk frequency diminishes as a function of distance from the cluster core, as found for the ONC by Getman et al. (2014), though some of this difference is likely due to the difference in X-ray sensitivity (Sections 4.1 and 4.4). While our statistics are not robust enough to provide a quantitative analysis of how the disks are distributed, we can qualitatively evaluate the distribution of disks through IC 1396-West, as depicted in Figure 4, keeping in mind the selection effects of the observed distribution due to the targeted nature of the Spitzer observations. We can also qualitatively assess the distribution of X-ray-identified likely cluster members through the nebula in conjunction.

We clearly see that disks tend to fall along the dust bands in the AllWISE data, which is borne out in the central Spitzer field (which had coverage in both I1 and I2)—more sources are identified in the central pointing of the Spitzer data, which falls on the nebula, and they generally tend to be disk sources. We note that the higher density of sources detected by Spitzer is due to its deeper observations—the faintest Spitzer sources in this field are an order of magnitude fainter in observed brightness than the faintest AllWISE sources.

There is a void of disk hosts and non-disk sources in the northern portion of the XMM-Newton field, save for a small group of disk sources in the upper corner that are not detected in X-rays, despite seemingly low nebular emission compared to the main "trunk." As fewer disks are expected in regions of lower nebular emission, the presence of these sources is intriguing. The group of disks seems potentially connected to a cluster of three X-ray sources without IR data (one in the cluster, two others unmatched to UKIRT), suggesting a filament of ongoing formation.

Surprisingly, many of the AllWISE-detected disk sources along the trunk are classified as Class I, the youngest type considered here. This suggests potential ongoing new star formation, extending the "triggered star formation" identified by Getman et al. (2012) to a farther distance from the cluster core. This supports the hypothesis of Pfalzner et al. (2014)—it will take longer for Class I YSO disks to evolve into Class II YSOs and then eventually dissipate their disks than it will take Class II YSO disks to dissipate, so the Class I disks identified here should remain present (albeit evolving) for an extended period of time.

There is also an intriguing band of X-ray-detected cluster members tracing the gap between the southern edge of the main trunk of the nebula and a smaller dust cloud. This range includes an X-ray-detected Class III source in a Spitzer field. The relative overabundance of X-ray-detected sources in this belt compared to the dust band above, combined with the higher concentration of disk sources along the belt, suggests that these sources are likely older, having already formed, evolved, and dissipated their disks. Similarly, the disks identified in this region are primarily Spitzer-detected Class II YSOs, suggesting a more evolved state of evolution than the Class I sources found along the dust band.

Pfalzner et al. (2014) hypothesized that disk fractions would be higher outside of the core of a massive cluster than in the cluster core, due in part to the enhanced contributions of external photoevaporation on the dissipation of the disk. However, Tr 37 and IC 1396 have an O-star binary at the core (HD 206267), which should contribute both to disk photoevaporation and dissipation of the nebula. We can see the nebular dissipation effects in the "bubble" appearance of the background gas and dust (Figure 1). However, the disk fraction we find here at a minimum indicates no increase in the disk fraction farther away from the cluster core. While our data are not robust enough to completely disprove this hypothesis, they do suggest that if there is a disk dissipation gradient, it is in the opposite direction of what Pfalzner et al. (2014) hypothesize.

4.4. Completeness of the X-Ray Luminosity Function

To determine the X-ray sensitivity of the XMM-Newton observation presented here, we converted the observed X-ray fluxes to luminosities using distances derived from Gaia parallaxes. Only 15 of our identified X-ray-detected cluster members have measured parallaxes, including 13 with mid-IR data; for the other 43 sources, we make the assumption that they are at the estimated cluster distance of 931 pc. The X-ray source with the fewest counts detected of the X-ray-detected cluster members (i.e., sources with both near-IR and X-ray detections and are not outside the cluster per Gaia) has X-ray flux $\sim 1.3 \times 10^{-15}$ erg s^{-1} cm^{-2} and distance 914^{+329}_{-159} pc, corresponding to an absorbed $\log L_X \approx 29.11$. For comparison, the faintest source with a determined L_X in Getman et al. (2012) has an unabsorbed $\log L_X = 28.99 \pm 0.17$ and an $\log(N_H) = 20.26 \pm 0.32$, which yields an absorbed $\log L_X \approx 28.95$. This indicates that the XMM observations are less sensitive than the adjacent Chandra field by 0.16 dex. We present our absorbed X-ray luminosity function (XLF) for both sources with mid-IR detections and the full set in comparison to the Getman et al. (2012) XLF in Figure 6. We also compare these XLFs against those of the Orion Nebula Cluster (the "cool unobscured" sample of cool stars with minimal optical extinction and X-ray absorption from Feigelson et al. 2005) and IC 348 (Stelzer et al. 2012).

Based on the comparison of our XLF to that of Getman et al. (2012), we estimate that the IC 1396-West sample is complete only to an unabsorbed $\log L_X \approx 30.8$, compared to the $\log L_X \approx 30.5$ completeness level in the IC 1396A field. Using the $L_X - M$ relation of Telleschi et al. (2007), this yields a minimum stellar mass of $1.8\,M_\odot$, well above the $1.0\,M_\odot$ of Getman et al. (2012) and thus explaining the qualitative discrepancy between X-ray-detected disk fractions for the two data sets; indeed, Ribas et al. (2015) note a clear difference in the rate of protoplanetary disk evolution (and thus disk lifetime) for $>2\,M_\odot$ stars compared to $<2\,M_\odot$ stars. We also note the similarity of the position of the XLF for both this observation of IC 1396 and that of Getman et al. (2012) to the XLF for IC 348, albeit not as complete at low L_X. We note that based on the exposure time for this XMM-Newton observation, to achieve completeness down to $\log L_X \approx 30.5$ would require a 174.5 ks observation, twice the length of the observation presented here.

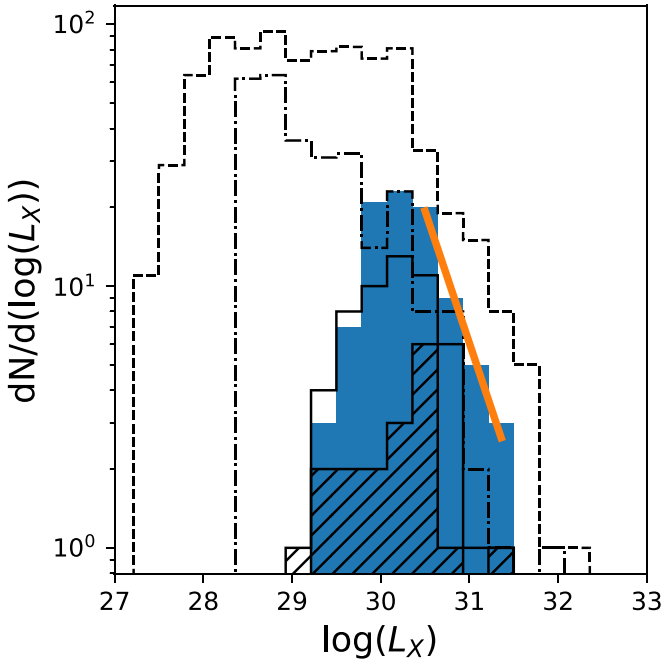

Figure 6. X-ray luminosity function of absorbed fluxes from X-ray-detected cluster members in IC 1396-West (solid line), in comparison to absorption-corrected fluxes from the adjacent IC 1396A field (blue). Hatched bars represent sources with mid-IR data in our sample. The orange line fits the approximate XLF of Getman et al. (2012). The XMM-Newton observations do not detect cluster members as faint as those in Getman et al. (2012). The XLF of 839 ONC stars (dashed lines; Feigelson et al. 2005, the "unobscured cool" sample) and IC 348 (dotted–dashed lines; Stelzer et al. 2012) are shown for comparison.

5. Spatial Structure of the IC 1396 Disk Distribution

The field observed with UKIRT/WFCAM fully overlaps with Chandra/ACIS-I observations of the cometary globule IC 1396A, presented in Getman et al. (2012). To foster a direct comparison of our methods to that paper, we applied our methodology to the IC 1396A field they observed, using their identifications of X-ray sources and the UKIRT/WFCAM data set to identify those objects that are likely cluster members. We note that as with the XMM-Newton data set, we use a 2″ search radius for matching all sources from Chandra to the UKIRT/WFCAM data set, while Getman et al. (2012) used a 2″ match radius in the center and a 3.″5 match radius further off axis to match their X-ray sources with 2MASS. In 27 instances, Getman et al. (2012) identified a 2MASS match to an X-ray source that did not have a UKIRT counterpart within 2″; these were cases where the X-ray source was off axis and the 2MASS match was between 2″ and 3.″5 away from the X-ray source. For these sources we searched for and identified a UKIRT counterpart to the 2MASS source, to ensure that we were evaluating approximately the same sources.

Getman et al. (2012) claimed 51 X-ray-detected disk hosts and 124 X-ray-detected non-disk-host cluster members, resulting in a disk fraction of 29^{+4}_{-3}%. By contrast, applying our methodology to the same field results in 38 X-ray-detected disk hosts and 75 X-ray-detected non-disk-host cluster members, resulting in a disk fraction of 33^{+5}_{-4}%.

We hypothesize that the difference in our estimated numbers of disk hosts and non-disk-host cluster members is due to our use of UKIRT/WFCAM data and Gaia EDR3 parallaxes, while Getman et al. (2012) used 2MASS data and estimated cluster membership based on color cuts and the X-ray data, because Gaia data were not available at their time of publication to provide an independent distance constraint. To check the effect of Gaia parallaxes, we independently estimated distances to their catalog of sources using Gaia EDR3 parallaxes. Getman et al. (2012) broke the X-ray source classifications in the Chandra field into six categories: DSK (a disk-hosting cluster member), EXG (extragalactic source), FRG (a foreground source), NOD (a non-disk-hosting cluster member), and UNC1 and UNC2 (two different types of uncertain member). Based on the 90% confidence intervals in distance for each object (using the same methodology for determining distances and distance uncertainties as Section 3 compared to the distance range derived in Section 2.4) we sorted objects in the Chandra field into six bins: in range (distance interval overlaps with the cluster distance); foreground (no overlap; entire confidence interval is in the foreground); background (no overlap; entire confidence interval is in the background); uncertain (overlaps, but with distance uncertainty ranges >1000 pc), no parallax (no parallax measured by Gaia), and 151 sources with no match between Chandra and UKIRT; while the majority of these come from the 219 sources in categories that had faint or no IR counterparts (EXG, UNC1, and UNC2), typically expected to be extragalactic (see Section 3.2 of Getman et al. 2012), some of these are also sources undetected in 2MASS/UKIRT but detected with Spitzer/IRAC. We present these results in Table 4 but focus our attention on the 121 sources in the "FRG," "DSK," and "NOD" classifications with UKIRT matches and Gaia parallaxes that yield a distance with uncertainty <1000 pc, as these are the most certain classifications.

We find that 90% of the DSK sources with UKIRT matches and Gaia EDR3-based distance uncertainties <1000 pc have distances consistent with the cluster distance. Similarly, 87% of the NOD sources with UKIRT matches have Gaia parallaxes consistent with the cluster distance. Only 67% of FRG sources are actually in the foreground, while four are at the correct distance for the cluster. We also find that our YSO-class assignments disagree in a handful of cases with those of Getman et al. (2012)—we classify three of their disk hosts as Class III YSOs and seven of their Class III YSOs as disk hosts. The remaining disks identified by our search that were not identified in Getman et al. (2012) emerge from the UNC1 and UNC2 bins, where the presence of UKIRT data and additional information from Gaia proves decisive. On the whole, while Gaia data does improve constraints on the distances, the classifications of Getman et al. (2012) are reasonably accurate, demonstrating the utility of this method of cluster member identification for clusters at distances where Gaia data is incomplete.

While the number of sources in IC 1396-West is small enough that a robust statistical comparison of the XMM-Newton field with the Chandra/ACIS-I field is infeasible, we can qualitatively compare these two regions, as well as the cluster core region analyzed by Mercer et al. (2009; which we do not reanalyze here due to that field falling outside the UKIRT field). The highest estimated fraction of X-ray-detected YSOs that have disks is that of Getman et al. (2012), which might suggest an increase in disk fraction from the cluster core to this field. However, we think it is more likely that this is because the observations analyzed by Mercer et al. (2009) were made with the HETG grating in place on Chandra, which significantly diminishes the efficiency of the observations and

Table 4.
Distance Assessments for Sources around IC 1396A from Getman et al. (2012) with Gaia EDR3

Category	Num. Sources	Foreground	In Range	Background	Uncertain	No Plx	No Match
DSK	51	2	26	1	9	9	4
EXG	29	0	0	0	2	21	6
FRG	21	10	4	1	4	1	1
NOD	124	6	69	4	33	8	4
UNC1	162	0	1	0	3	31	127
UNC2	28	2	3	0	7	7	9

Note. Category definitions: DSK: disk-hosting source; EXG: extragalactic source; FRG: foreground; NOD: non-disk-host cluster member; UNC1: uncertain origin, likely extragalactic; UNC2: uncertain origin, possible YSOs.

likely led to nondetection of some sources. Overall, the data indicate that the disk fraction does not increase as a function of distance from the cluster core. Future work with deeper X-ray observations will be necessary to fully quantify this effect in clusters other than the ONC.

6. Summary

In this paper, we present X-ray detections from an 87.3 ks exposure with the XMM-Newton Observatory, which we combine with near-infrared wide-field images with UKIRT/WFCAM and archival data from Gaia EDR3, Spitzer, and AllWISE to identify disk-hosting and non-disk-hosting young stars forming in a field at the western edge of the Elephant's Trunk Nebula, which we designate as IC 1396-West. We also used Gaia EDR3 to reevaluate the color-cut-based YSO identification scheme of Getman et al. (2012) for Chandra observations of the field surrounding the cometary globule IC 1396A. We find the following:

1. We identify 421 new members of the Tr 37/IC 1396A cluster, including 86 Class I YSOs (one detected in X-rays), 51 Class FS YSOs (one detected in X-rays), 229 Class II YSOs (one detected in X-rays), 15 Class III YSOs (all detected in X-rays), and 40 sources with X-ray detections but no mid-IR data to determine a YSO class.
2. The disk fraction of X-ray-detected YSOs in IC 1396-West is 17^{+10}_{-7}%, statistically consistent with the 29^{+4}_{-3}% rate for an adjacent region closer to the core of IC 1396, centered on the globular cluster IC 1396A and observed with Chandra ACIS-I (Getman et al. 2012). The XMM-Newton X-ray observations do not probe to as deep of a luminosity as the Chandra observations of IC 1396A, which leads to those observations extending to lower completeness than the XMM-Newton observations here. The small number of sources detected, due in part to both the difference in completeness of the observations and the lower sensitivity of the mid-IR data for most of IC 1396-West (mostly WISE) compared to the IC 1396A field (fully observed by Spitzer), makes any difference statistically insignificant. This result also does not consider lower-mass stars too faint to be detected in the XMM-Newton or Chandra/ACIS observations that retain their disk longer than the higher-mass stars we detect in X-rays.
3. We note a surprising number of Class I YSOs along the nebula, suggesting ongoing star formation in this region later than the birth of stars in Tr 37.
4. While color-cut-based searches for YSOs in clusters without distance information is reasonably effective, the addition of independent distance measurements provides key additional constraints on YSO identification. We find from our reanalysis of the field of Chandra observations of IC 1396A that the disk fraction following our methodology is 33^{+5}_{-4}%, comparable with the 29^{+4}_{-3}% rate derived by Getman et al. (2012).

While the additional information provided by Gaia was invaluable to us in our search for Class III YSOs, it was not entirely conclusive, as Gaia parallaxes are not complete to the distance of Tr 37, especially with particularly dense background emission from the nebula. We expect that future releases from Gaia will yield parallax information for more stars, which will provide better identification of Class III sources—in particular, those sources with photospheric SED slopes and detected X-ray emissions but no parallax measurements. This improved completeness will also enable more effective determination of what fraction of sources with photospheric SEDs at the correct distance but are not detected in X-rays are likely to be members of the cluster, which will further improve estimates of the age of clusters by extending membership lists to lower luminosities.

Even after the end of its mission, the Gaia data set will have limitations that can be overcome by the use of multiple observation methods. The X-ray observations we collected here show a set of potential YSOs (based on their position relative to the nebula and their X-ray hardness ratios) that went unidentified by Gaia, demonstrating the utility of an approach that combines data from Gaia and other observatories. As the large X-ray catalog from the eROSITA mission (Predehl et al. 2014) becomes available, these data will be crucial for helping to identify the objects that are missed by Gaia, helping us build a more comprehensive picture of the formation and evolution of young stellar objects.

We thank the anonymous reviewer for providing comments that helped to improve the content and clarity of this paper. The authors thank Aurora Sicilia-Aguilar for valuable discussions on estimating the distance to IC 1396. The authors thank Nicholas J. G. Cross for helpful comments on the WFCAM archive. S.M.S. and H.M.G. were supported by the National Aeronautics and Space Administration through Chandra Award Number GO9-20019X issued by the Chandra X-ray Observatory Center, which is operated by the Smithsonian Astrophysical Observatory for and on behalf of the National Aeronautics Space Administration under contract NAS8-03060. S.J.W. was supported by NASA contract NAS8-03060.

When the data reported here were acquired, UKIRT was supported by NASA and operated under an agreement among

the University of Hawaii, the University of Arizona, and Lockheed Martin Advanced Technology Center; operations were enabled through the cooperation of the East Asian Observatory. UKIDSS uses the UKIRT Wide Field Camera (WFCAM; Casali et al. 2007) and a photometric system described in Hewett et al. (2006). The pipeline processing and science archive are described in Hambly et al. (2008).

This work is based in part on observations made with the Spitzer Space Telescope, which is operated by the Jet Propulsion Laboratory, California Institute of Technology under a contract with NASA.

This publication makes use of data products from the Wide-field Infrared Survey Explorer, which is a joint project of the University of California, Los Angeles, and the Jet Propulsion Laboratory/California Institute of Technology, funded by the National Aeronautics and Space Administration.

This research has made use of the NASA/IPAC Infrared Science Archive, which is funded by the National Aeronautics and Space Administration and operated by the California Institute of Technology.

This work has made use of data from the European Space Agency (ESA) mission Gaia (https://www.cosmos.esa.int/gaia), processed by the Gaia Data Processing and Analysis Consortium (DPAC, https://www.cosmos.esa.int/web/gaia/dpac/consortium). Funding for the DPAC has been provided by national institutions, in particular the institutions participating in the Gaia Multilateral Agreement.

This research has made use of the SIMBAD database, operated at CDS, Strasbourg, France. This research has made use of the VizieR catalog access tool, CDS, Strasbourg, France. This research made use of the crossmatch service provided by CDS, Strasbourg.

This publication makes use of data products from the Two Micron All Sky Survey, which is a joint project of the University of Massachusetts and the Infrared Processing and Analysis Center/California Institute of Technology, funded by the National Aeronautics and Space Administration and the National Science Foundation.

Facilities: IRSA, Spitzer, WISE, UKIRT/WFCAM, XMM-Newton

Software: AstroPy (Astropy Collaboration et al. 2013, 2018), NumPy (Van Der Walt et al. 2011; Harris et al. 2020), SciPy (Virtanen et al. 2020), Matplotlib (Hunter 2007), pandas (McKinney 2010; Reback & McKinney 2020).

ORCID iDs

Steven M. Silverberg https://orcid.org/0000-0002-3741-4181
Hans Moritz Günther https://orcid.org/0000-0003-4243-2840
Jinyoung Serena Kim https://orcid.org/0000-0001-6072-9344
David A. Principe https://orcid.org/0000-0002-7939-377X
Scott J. Wolk https://orcid.org/0000-0002-0826-9261

References

Anderson, K. R., Adams, F. C., & Calvet, N. 2013, ApJ, 774, 9
Astropy Collaboration, Robitaille, T. P., Tollerud, E. J., et al. 2013, A&A, 558, A33
Astropy Collaboration, Price-Whelan, A. M., Sipőcz, B. M., et al. 2018, AJ, 156, 123
Bailer-Jones, C. A. L. 2015, PASP, 127, 994
Bailer-Jones, C. A. L., Rybizki, J., Fouesneau, M., Mantelet, G., & Andrae, R. 2018, AJ, 156, 58
Barentsen, G., Vink, J. S., Drew, J. E., et al. 2011, MNRAS, 415, 103
Booth, R. S., Poppenhaeger, K., Watson, C. A., Silva Aguirre, V., & Wolk, S. J. 2017, MNRAS, 471, 1012
Carpenter, J. M., Mamajek, E. E., Hillenbrand, L. A., & Meyer, M. R. 2006, ApJL, 651, L49
Casali, M., Adamson, A., Alves de Oliveira, C., et al. 2007, A&A, 467, 777
Contreras, M. E., Sicilia-Aguilar, A., Muzerolle, J., et al. 2002, AJ, 124, 1585
Cutri, R. M., Wright, E. L., Conrow,, T., et al. 2021, VizieR Online Data Catalog, II/328
Feigelson, E. D., Getman, K., Townsley, L., et al. 2005, ApJS, 160, 379
Fressin, F., Torres, G., Charbonneau, D., et al. 2013, ApJ, 766, 81
Gaia Collaboration, Brown, A. G. A., Vallenari, A., et al. 2021, A&A, 649, A1
Gaia Collaboration, Prusti, T., de Bruijne, J. H. J., et al. 2016, A&A, 595, A1
Getman, K. V., Feigelson, E. D., Garmire, G., Broos, P., & Wang, J. 2007, ApJ, 654, 316
Getman, K. V., Feigelson, E. D., & Kuhn, M. A. 2014, ApJ, 787, 109
Getman, K. V., Feigelson, E. D., Sicilia-Aguilar, A., et al. 2012, MNRAS, 426, 2917
Ginsburg, A., Sipőcz, B. M., Brasseur, C. E., et al. 2019, AJ, 157, 98
Günther, H. M., Wolk, S. J., Spitzbart, B., et al. 2012, AJ, 144, 101
Güver, T., & Özel, F. 2009, MNRAS, 400, 2050
Haisch, Karl E., J., Lada, E. A., & Lada, C. J. 2001, ApJL, 553, L153
Hambly, N. C., Collins, R. S., Cross, N. J. G., et al. 2008, MNRAS, 384, 637
Harris, C. R., Millman, K. J., van der Walt, S. J., et al. 2020, Natur, 585, 357
Hewett, P. C., Warren, S. J., Leggett, S. K., & Hodgkin, S. T. 2006, MNRAS, 367, 454
Hughes, A. M., Duchêne, G., & Matthews, B. C. 2018, ARA&A, 56, 541
Hunter, J. D. 2007, CSE, 9, 90
Irwin, J., Charbonneau, D., Nutzman, P., & Falco, E. 2009, in IAU Symp. 253, Transiting Planets, ed. F. Pont, D. Sasselov, & M. J. Holman (Cambridge: Cambridge Univ. Press), 37
Kennedy, G. M., & Wyatt, M. C. 2012, MNRAS, 426, 91
Kuchner, M. J., Silverberg, S. M., Bans, A. S., et al. 2016, ApJ, 830, 84
Kun, M., Kiss, Z. T., & Balog, Z. 2008, in Star Forming Regions in Cepheus, ed. B. Reipurth, Vol. 4 (San Francisco, CA: ASP), 136
Kunimoto, M., & Matthews, J. M. 2020, AJ, 159, 248
Lada, C. J. 1987, in IAU Symp. 115, Star Forming Regions, ed. M. Peimbert & J. Jugaku (Cambridge: Cambridge Univ. Press), 1
McKinney, W. 2010, in Proc. 9th Python in Science Conf., ed. S. van der Walt & J. Millman, 51
Meng, H. Y. A., Rieke, G. H., Kim, J. S., et al. 2019, ApJ, 878, 7
Mercer, E. P., Miller, J. M., Calvet, N., et al. 2009, AJ, 138, 7
Morales-Calderón, M., Stauffer, J. R., Rebull, L., et al. 2009, ApJ, 702, 1507
Moretti, A., Campana, S., Lazzati, D., & Tagliaferri, G. 2003, ApJ, 588, 696
Pecaut, M. J., & Mamajek, E. E. 2013, ApJS, 208, 9
Pecaut, M. J., & Mamajek, E. E. 2016, MNRAS, 461, 794
Pfalzner, S., Steinhausen, M., & Menten, K. 2014, ApJL, 793, L34
Predehl, P., Andritschke, R., Becker, W., et al. 2014, Proc. SPIE, 9144, 91441T
Preibisch, T., & Feigelson, E. D. 2005, ApJS, 160, 390
Reach, W. T., Rho, J., Young, E., et al. 2004, ApJS, 154, 385
Reback, J., & McKinney, W. 2020, pandas-dev/pandas: Pandas, v1.0.1, Zenodo, doi:10.5281/zenodo.3644238
Ribas, Á., Bouy, H., & Merín, B. 2015, A&A, 576, A52
Robitaille, T. P. 2017, A&A, 600, A11
Robitaille, T. P., Whitney, B. A., Indebetouw, R., Wood, K., & Denzmore, P. 2006, ApJS, 167, 256
Sicilia-Aguilar, A., Hartmann, L. W., Fürész, G., et al. 2006a, AJ, 132, 2135
Sicilia-Aguilar, A., Hartmann, L. W., Hernández, J., Briceño, C., & Calvet, N. 2005a, AJ, 130, 188
Sicilia-Aguilar, A., Kim, J. S., Sobolev, A., et al. 2013, A&A, 559, A3
Sicilia-Aguilar, A., Patel, N., Fang, M., et al. 2019, A&A, 622, A118
Sicilia-Aguilar, A., Hartmann, L. W., Szentgyorgyi, A. H., et al. 2005b, AJ, 129, 363
Sicilia-Aguilar, A., Hartmann, L., Calvet, N., et al. 2006b, ApJ, 638, 897
Silverberg, S. M., Kuchner, M. J., Wisniewski, J. P., et al. 2018, ApJ, 868, 43
Skrutskie, M. F., Cutri, R. M., Stiening, R., et al. 2006, AJ, 131, 1163
Stelzer, B., Preibisch, T., Alexander, F., et al. 2012, A&A, 537, A135
Sung, H., Stauffer, J. R., & Bessell, M. S. 2009, AJ, 138, 1116
Telleschi, A., Güdel, M., Briggs, K. R., Audard, M., & Palla, F. 2007, A&A, 468, 425
Van Der Walt, S., Colbert, S. C., & Varoquaux, G. 2011, CSE, 13, 22
Virtanen, P., Gommers, R., Oliphant, T. E., et al. 2020, NatMe, 17, 261
Werner, M. W., Roellig, T. L., Low, F. J., et al. 2004, ApJS, 154, 1
Williams, J. P., & Cieza, L. A. 2011, ARA&A, 49, 67
Wilson, E. B. 1927, J. Am. Stat. Ass., 22, 209
Wolk, S. J., Spitzbart, B. D., Bourke, T. L., et al. 2008, AJ, 135, 693
Wright, E. L., Eisenhardt, P. R. M., Mainzer, A. K., et al. 2010, AJ, 140, 1868